



# Analysis of multi-mode waveguide cavities containing free space gaps for use in future far-infrared telescopes



Darragh McCarthy<sup>a</sup>, Neil Trappe<sup>a,\*</sup>, Stephen Doherty<sup>b</sup>, J. Anthony Murphy<sup>a</sup>, Marcin Gradziel<sup>a</sup>, Colm Bracken<sup>c</sup>, Cr  idhe O'Sullivan<sup>a</sup>, Michael D. Audley<sup>d</sup>, Gert de Lange<sup>d</sup>, Maarten van der Vorst<sup>e</sup>

<sup>a</sup> *Maynooth University, Department of Experimental Physics, Maynooth, Co. Kildare, Ireland*

<sup>b</sup> *ViaSat Antenna Systems SA, Lausanne, Switzerland*

<sup>c</sup> *Dublin Institute for Advanced Studies, 31 Fitzwilliam Place, Dublin 2, Ireland*

<sup>d</sup> *Space Research Organisation of the Netherlands (SRON), Groningen, the Netherlands*

<sup>e</sup> *ESTEC, European Space Agency (ESA), Noordwijk, the Netherlands*

## ARTICLE INFO

### Keywords:

Far-infrared  
Horn antennas  
Integrating cavity  
Mode matching  
Transition edge sensor  
Multi-mode

## ABSTRACT

In order to investigate the formation and evolution of galaxies, stars and planetary systems, it is necessary to carry out astronomical observations in the far-infrared portion of the electromagnetic spectrum. Missions such as the Herschel Space Observatory (European Space Agency) have already completed observations in this region with great success. Proposed high resolution spectrometer instruments such as SAFARI (a joined European/Japanese (ESA/JAXA) proposal as part of the SPICA mission), aim to build upon the work of previous missions by carrying out observations in the 1.5–10 THz band with unprecedented levels of sensitivity. Spica (SPace Infrared telescope for Cosmology and Astrophysics) is currently a candidate mission as part of ESA's Cosmic Vision 2015–2025.

Future far-IR missions must realise higher levels of sensitivity, limited only by the cosmic microwave background. One solution in achieving these sensitivity goals is to use waveguide coupled Transition Edge Sensor (TES) detectors, arranged in a densely packed focal plane. Additionally, multi-mode pixels can be used in order to maximise the optical throughput and coupling while still defining a definite beam shape. For the SAFARI instrument multimoded horns coupling into integrating waveguide cavities that house the TES detectors and associated absorbing layer are envisioned. This represents a significant technological challenge in terms of accurate manufacture tolerances relative to the short wavelength, however in the case of the SAFARI instrument pixel much work has already been carried out, with prototype pixels having undergone extensive testing at SRON (Space Research Organisation of the Netherlands) Groningen. In order to fully characterise the experimental results, it is necessary also to carry out comprehensive electromagnetic modelling of these structures which is also computationally intensive and requires novel approaches. These waveguide structures (horn and cavity) are typically electrically large however, and so analysis techniques using commercial finite element software prove inefficient (particularly as the structures are multimoded).

The mode-matching technique with new analytical features offer a computationally efficient and reliable alternative to full electromagnetic solvers, and in this paper we outline the additions to this technique that were necessary in order to allow typical SAFARI far-infrared pixels to be modeled, including the complete optical coupling calculation of the measurement test setup at SRON and the inclusion of the free space gap within the horn antenna and the integrating cavity. Optical coupling efficiencies simulated using this developed technique show excellent agreement with the experimental measurements.

## 1. Introduction

Future far infrared space telescopes have a wide variety of scientific

objectives, aiming to build upon the work carried out by previous missions such as the Herschel Space Observatory [1]. An example of such a future mission is the proposed SPICA (SPace Infrared telescope

\* Corresponding author.

E-mail address: [neal.a.trappe@mu.ie](mailto:neal.a.trappe@mu.ie) (N. Trappe).

URL: <https://www.maynoothuniversity.ie/experimental-physics/our-people/neil-trappe/> (N. Trappe).

<https://doi.org/10.1016/j.infrared.2020.103235>

Received 6 January 2020; Accepted 9 February 2020

Available online 14 February 2020

1350-4495/   2020 Elsevier B.V. All rights reserved.

for Cosmology and Astrophysics) mission [2,3], a collaboration between Europe and Japan (ESA and JAXA). The SAFARI (SPICA FAR Infrared Instrument) instrument, an imaging high resolution grating spectrometer, is planned to fly onboard the SPICA mission. SAFARI is optimised to operate in the 1.5–10 THz band, utilising the low background environment provided by the cooled SPICA telescope that is limited only by the cosmic microwave background (CMB) radiation to study the formation and evolution of galaxies, stars and planetary systems.

If the results obtained from previous missions are to be improved upon, it is necessary for future instruments to realise higher levels of sensitivity, allowing the complete exploitation of the extraordinary sensitivity permitted by the cold telescope optics and sensitive superconducting detectors (Transition Edge Sensors (TES)).

Sensitivity can be maximised by utilising a focal plane with a high packing density and by using multi-mode horns to feed the transition edge sensors and associated absorber in a waveguide cavity in order to maximise optical coupling. This has been demonstrated at SRON (Space Research Organisation of the Netherlands) Groningen, where extremely sensitive detector pixels have been developed and characterised for the SAFARI instrument, as reported in [4,5]. A schematic diagram of the waveguide pixel developed at SRON is shown in Fig. 1, where the drawing is not to scale. For clarity, due to the length of the feed horn, only a short section of the horn (a smooth-walled conical horn) is shown. The integrating cavity is placed behind the focal plane horn (to be part of an array ultimately). Due to the horn and backend cavity housing the TES being manufactured separately a free space gap is necessary and must be included in all optical analysis. In waveguide pixels such as these, a multi-mode conical feed horn feeds a cavity that contains the absorber with the TES - a thin tantalum superconducting absorbing layer of material. The power absorbed by this layer is measured by means of a TES detector. This overall waveguide geometry increases the efficiency of the pixel in two ways. Being a multi-moded system there are more channels of power supported and so the

sensitivity is immediately increased due to the higher modal throughput per pixel. The presence of the cavity also boosts the pixel optical coupling by trapping any incident power that is not absorbed on the first pass of the tantalum layer, reflecting it and forcing it to undergo several additional passes of the tantalum. This means that a higher percentage of the power incident on the pixel is potentially absorbed in such a waveguide cavity.

Such systems are challenging to model electromagnetically, in particular due to the necessity to include additional features such as a free space gap that exists between the metal horn array and the cavity array that is manufactured separately on a silicon wafer (which exists as the two arrays clearly cannot be manufactured monolithically, and also to maintain structural integrity during launch). Software packages such as Computer Simulation Technology Microwave Studio (CST MWS) and COMSOL are of course capable of modelling such systems, however at the frequencies in question these structures are electrically large and so it is not feasible for most research groups to model anything other than smaller representative models, given the computing resources that are typically available. Therefore, in order to design, optimise and analyse pixels for future instruments that operate in the 1.5–10 THz band, it is necessary to develop alternative efficient and reliable modelling and analysis tools and techniques.

The mode-matching technique, originally described in [6], allows the electromagnetic and optical performance of waveguide structures to be simulated, and can be applied to complex focal plane pixels. In this paper we outline an extension of this technique to include the elements necessary to model the terahertz pixels in question such as absorbing layers and free space gaps between waveguide structures. The techniques can of course be applied to pixels at any wavelength that utilise these elements. We apply this model of the pixels to the testbed that was used in SRON Groningen and outline the additional steps that were necessary to fully simulate the test setup, extracting simulated values for the detected power and comparing them to the measured values in an integrated frequency band.

## 2. Modelling and analysis techniques

In this section the mode-matching technique is described alongside the implementation of the additional features that are necessary to include to analyse the test pixels outlined in Section 1.

### 2.1. The mode-matching technique

The mode-matching technique is a powerful analytical tool that can be used to analyse the full vector electromagnetic performance of waveguide structures. At Maynooth University this technique has been studied extensively, resulting in the in-house development of software referred to as SCATTER [7,8] that allows the analysis of two port systems of either rectangular or circular cross-section, where the waveguide material is assumed to be perfectly electrically conducting. SCATTER refers to the collected modematching techniques as an integrated programme developed in various software platforms (C++, Python, Mathematica etc) developed as a software tool at Maynooth University building on the modelling heritage [8]. In this platform SCATTER represents the fields propagating in the structures in question as combinations of transverse electric (TE) and transverse magnetic (TM) modes, calculating the scattering matrices (the well known S-matrices, [6]) that govern the scattering between these modes in any plane where the cross-sectional dimensions of the structure changes. In this manner, a set of scattering matrices can be calculated which governs the bulk response of the waveguide structure to any given excitation. Using these scattering matrices the field patterns of the structure (in the aperture plane and the farfield) can be calculated, along with all of the scattering parameters of the system. This can be used to examine the performance of the structures by calculating relevant parameters such as beam ellipticity, sidelobe levels, reflections,

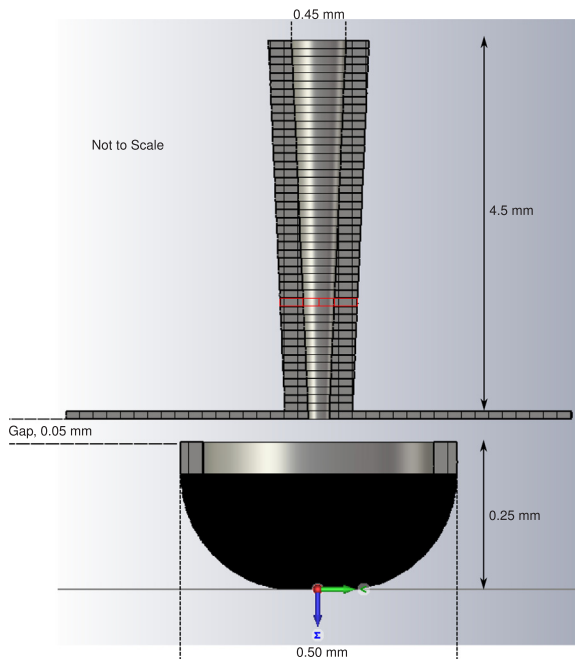


Fig. 1. Schematic of the pixel tested at SRON (dimensions in mm). The smooth-walled conical horn has a throat radius of 0.05 mm. This pixel is designed to operate in the 4.3–8.5 THz band for test purposes. The array of horns can be formed by drilling several feed horns into a metal block, adjacent to one another, and placing this block over an array of cavities that are manufactured separately on a silicon wafer. Wire cut pyramidal horns are also being investigated.

modal content, optical efficiency etc. SCATTER has been extensively verified, both experimentally and by benchmarking against software packages such as CST MWS, in both single and multi-mode operation, as reported in [7].

## 2.2. Including an absorbing layer in the mode-matching technique

The absorbing material that is located in the cavity section of the pixel is represented in the mode-matching technique by means of an infinitely thin ohmic sheet. This is implemented by imposing appropriate boundary conditions on the electric and magnetic fields propagating across the sheet as shown in (1)–(3)

$$\mathbf{E}_L = \mathbf{E}_R \quad (1)$$

$$\mathbf{H}_L = \mathbf{H}_R - \mathbf{K} \times \hat{k} \quad (2)$$

$$\mathbf{K} = \frac{\mathbf{E}_L}{R_s} = \frac{\mathbf{E}_R}{R_s}, \quad (3)$$

where the subscripts  $L$  and  $R$  refer to the left and right hand sides of the ohmic sheet respectively and  $R_s$  is the impedance of the ohmic sheet in units of Ohms per square. By using these boundary conditions alongside the standard mode-matching procedure, the scattering matrices that govern the behaviour of the sheet are found to be

$$S_{11} = S_{22} = \left[ \mathbf{Q}^* + \frac{\mathbf{Z} \cdot \mathbf{P}}{2R_s} \right]^{-1} \cdot \frac{\mathbf{Z} \cdot \mathbf{P}}{2R_s} \quad (4)$$

$$S_{12} = S_{21} = \left[ \mathbf{Q}^* + \frac{\mathbf{Z} \cdot \mathbf{P}}{2R_s} \right]^{-1} \cdot \mathbf{Q}^*, \quad (5)$$

where  $\mathbf{Z}$  represents the impedance of the waveguide mode that the calculation is being performed for,  $\mathbf{P}$  is a matrix representing the coupling of the waveguide modes across the ohmic sheet and  $\mathbf{R}$  and  $\mathbf{Q}$  are matrices representing the self coupling (reflections) of the waveguide modes on the left and right sides of the sheet respectively. This concept is also explored in an alternate framework in [9]

If an ohmic sheet is included in any mode-matching model, the power absorbed by the sheet can be determined by a careful examination of the scattering matrices. In pixels such as those under test at SRON, one end of the system is a closed cavity that acts as a back-short. Since power can therefore only enter and exit the system through one port (assuming lossless waveguides), the  $S_{11}$  matrix is the only matrix containing any power. If an ohmic sheet is included in the model, the absorbed power is determined therefore by comparing the power used to excite the system and the power contained in the  $S_{11}$  matrix, with the difference being the absorbed power.

If the  $S_{11}$  matrix is analysed using singular value decomposition (SVD), an approach considered in [10,11], then three matrices are returned such that  $S_{11} = U \cdot \Sigma \cdot V^\dagger$ . The columns of  $U$  define a more compact basis set for the output mode set of the system.  $\Sigma$  is a diagonal matrix that give the singular values of the system,  $\sigma_i$ , such that  $\sigma_i = \Sigma_{ii}$ . These singular values scale the corresponding mode (the  $i$ th column of  $U$ ) such that  $\sigma_i^2$  gives the fraction of the input power that the corresponding mode was excited with (unity in SCATTER) which arrives back at the port following propagation through the system. Since the singular values scale the output modes, only modes with non-zero singular values are supported by the system. This allows the system to be analysed in a highly efficient manner due to the reduced number of optimised modes, with no compromise in accuracy [11]. Since each mode is excited with unity power,  $\sigma_i^2$  directly gives the power that exits the pixel, and so the power absorbed by the Ohmic sheet is given by  $1 - \sigma_i^2$ . If the pixel supports  $\beta$  modes, then the total absorbed power is given by

$$P_{\text{Tot}} = \beta - \sum_{i=1}^{\beta} \sigma_i^2. \quad (6)$$

## 2.3. Including a free space gap in the mode-matching technique

For an accurate model of the pixel, it is necessary to include the 50  $\mu\text{m}$  gap between the feed horn and the cavity as in Fig. 1. As the modes propagate across this gap they will increase in spatial extent due to diffraction and so some power will ‘leak’ from the system. This will alter the performance of the pixel and so this effect must be quantified. Additionally, this leaked power could potentially appear as crosstalk in neighbouring pixels when the pixels are used in an array, and so it will be useful in the future to account for this during the design process. Since the gap is treated as being in free space, and the pixels in question are circular in cross-section, Gaussian-Laguerre modes, [12], are the most appropriate mode set for representing the scalar fields that propagate across the gap. This mode set is given by

$$\begin{aligned} \left( \begin{array}{c} \Psi_m^{\alpha, \cos}(r, \phi, z) \\ \Psi_m^{\alpha, \sin}(r, \phi, z) \end{array} \right) &= \sqrt{\frac{2(2 - \delta_{0\alpha})m!}{\pi W^2(m + \alpha)!}} \exp\left(\frac{-r^2}{W^2}\right) \times \\ \left( \frac{2r^2}{W^2} \right)^{\frac{\alpha}{2}} L_m^\alpha\left(\frac{2r^2}{W^2}\right) \exp\left(-jk\left(\frac{r^2}{2R}\right)\right) \times \\ &\exp(-j(kz - \phi_{m,\alpha(z)})) \begin{pmatrix} \cos\alpha\phi \\ \sin\alpha\phi \end{pmatrix}, \end{aligned} \quad (7)$$

where  $L_m^\alpha$  is an Associated Laguerre polynomial of order  $m$  and degree  $\alpha$ .  $W$ ,  $R$  and  $\phi_{m,\alpha}$  represent the width, phase radius of curvature and phase slippage of each of the free space modes and their values are tracked across the gap using standard ABCD techniques. Using this scalar approach, the field in any plane across the gap can be readily calculated, [12]. The process for transforming between circular TE and TM modes and Gaussian-Laguerre modes is described in [13]. This allows the transformation into free space at the horn throat and the subsequent transformation into waveguide modes at the cavity to be accounted for completely. It should be noted that the coupling to free space for a particular waveguide mode and its orthogonal polarisation is the same, so the calculation does not need to be carried out for each polarisation. Additionally, since the Laguerre-Gaussian modes are solutions to the paraxial scalar wave equation, the co and cross-polar components of the waveguide modes must be individually coupled into the free space modes and a sufficient number of modes must be used in order to ensure an accurate representation of the propagating fields at larger off-axis positions.

## 2.4. Including a truncating section and reflective plate in the mode-matching technique

A schematic representation of the SAFARI pixel under consideration is shown in Fig. 2, where the drawing is not to scale for clarity. The reflective plate and truncating sections are additional elements that are required to fully model the gap, in addition to those already outlined. As the free space modes propagate across the gap, the amount of power located off-axis in a given mode will increase as the modes spread out

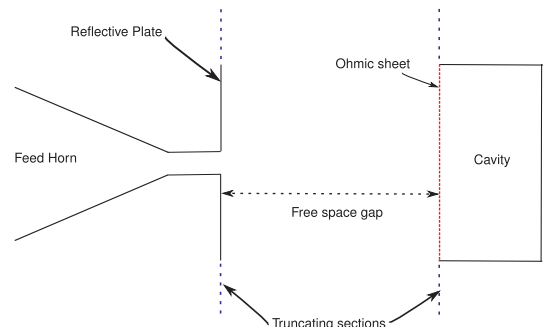


Fig. 2. Schematic of a pixel that is a general version of the SAFARI pixels tested at SRON, adapted from [14].

due to diffraction. In many cases, the amount of power located off-axis beyond the extent of the pixel will be non-negligible. This power cannot couple back into the horn or cavity and so becomes the leaked power, however SCATTER forces power to be conserved and so will not account for this. The truncating sections allow this effect to be included as an additional loss mechanism within the system (free space walkoff).

The truncating section is defined as an infinitely thin annulus, with a gap in the centre equal in size to the horn throat or cavity opening, and extending beyond this infinitely (so as to absorb all power that falls beyond the extent of the pixel), as in Fig. 2. It is assumed that no reflections occur in the plane of the truncating section; power incident on the gap is entirely transmitted and all other power is absorbed. In the mode-matching approach, matrices of coefficients are used to represent the transmitted and reflected fields. Following the convention used in [6],  $B$  and  $D$  are matrices which represent the reflected modes. Since it is assumed that there are no reflections, if  $N$  free space modes are used and  $e^+$  and  $e^-$  represent the free space fields travelling in the forward (left to right in Fig. 2) and reverse directions respectively, we have that  $\sum_{n=1}^N B_n e_n^- = 0$  and  $\sum_{n=1}^N D_n e_n^+ = 0$ . Using this along with the standard continuity conditions for the electric and magnetic fields across the sheet [6], it can be shown that

$$P_1 A + P_2 B = P_2 C + P_1 D \quad (8)$$

$$-P_1 A + P_2 B = P_2 C - P_1 D \quad (9)$$

$$Q_2 B = 0 \quad (10)$$

$$Q_1 D = 0. \quad (11)$$

$A$  and  $C$  are matrices containing the coefficients of the modes in transmission.  $P$  and  $Q$  are matrices populated by evaluating

$$P_{1,ij} = \int_0^R e_i^+ \cdot e_j^+ 2\pi r dr \quad (12)$$

$$P_{2,ij} = \int_0^R e_i^- \exp\left(\frac{jkr^2}{2R}\right) \cdot e_j^- 2\pi r dr \quad (13)$$

$$Q_{1,ij} = \int_R^\infty e_i^+ \cdot e_j^+ 2\pi r dr \quad (14)$$

$$Q_{2,ij} = \int_R^\infty e_i^- \exp\left(\frac{jkr^2}{2R}\right) \cdot e_j^- 2\pi r dr, \quad (15)$$

where  $R$  represents the radius of either the horn throat or the cavity, depending on which side of the gap is in question. Additionally, by conservation of complex power, we must have that  $P_1 + Q_1 = \mathbb{I}$  and  $P_2 + Q_2 = \mathbb{I}$ , where  $\mathbb{I}$  represents an appropriately dimensioned identity matrix.

Solving 8 and 9 simultaneously yields  $P_2 B = P_2 C$  and  $P_1 A = P_1 D$ . Using these equations alongside 10, 11 and the conservation identities above gives that  $D = P_1 A$  and  $B = P_2 C$ . Following the convention used in [6], the scattering matrices that determine the behaviour of the truncating section are given by

$$\begin{aligned} S_{11} &= 0 \\ S_{12} &= P_2 \end{aligned} \quad (16)$$

$$\begin{aligned} S_{21} &= P_1 \\ S_{22} &= 0. \end{aligned}$$

The purpose of the reflective gap is to simulate the reflective surface presented to the modes in the gap region when they arrive back at the horn having traversed the cavity/gap. This surface exists as the horns are machined into a solid block and so the space between adjacent pixels consists of the bare block. This surface must be included in the model, as it traps power within the pixel rather than allowing it to leave the system around the horn. It is implemented in a similar manner as the truncating section outlined above. In the area of the horn throat, the standard continuity conditions outlined in [6] are still valid. For radii beyond that of the horn throat, the continuity condition is given by

$$\sum_n^N D_n \cdot e_n^+ = - \sum_n^N C_n \cdot e_n^-, \quad (17)$$

where  $[A]$  and  $[B]$  are zero in this region, as the material is a perfect reflector. Following the same procedure as for the truncating section, the scattering matrices for the reflective section are found to be given by

$$\begin{aligned} S_{11} &= 0 \\ S_{12} &= P_2 \end{aligned} \quad (18)$$

$$\begin{aligned} S_{21} &= P_1 \\ S_{22} &= -Q_2. \end{aligned}$$

With these scattering matrices calculated, the free space transition, and the truncating/reflective sections can now be included as an integrated part of a model of the pixel that is being simulated using the mode-matching technique. The validity of this model was verified by applying it to a pixel containing a sealed cavity, designed for 70 GHz operation. Excellent agreement with CST MWS was obtained, [14], and so the model can be applied with confidence to SAFARI-like pixels that operate at significantly higher frequencies.

### 2.5. Coupling the pixel to the measurement system

In order to use the model outlined previously to obtain values for absorbed power that are comparable to the values measured at SRON, it is necessary to couple the pixel model to the SRON optical measurement system, a schematic of which is shown in Fig. 3 and described in detail in [4,5]. In the SRON measurement setup, a conical black-body radiator is used to illuminate a pinhole aperture via a series of band defining filters, with the pixel located behind this pinhole aperture. The pixel efficiency, which was measured at SRON, is defined as the ratio of the detected power to the power incident on the cavity portion of the pixel and so it is heavily dependant on the experimental configuration which can be varied by altering the size of the pinhole aperture ( $D_{BB}$ ) and the distance from this plane to the pixel's conical horn ( $L_{BB}$ ).

Considering an arbitrary system configuration (arbitrary values for  $D_{BB}$  and  $L_{BB}$ ), we begin by calculating the amount of power that arrives at the entrance aperture of the pixel from the pinhole aperture, assuming that the true modes of the pixel have already been calculated using SVD and are represented by  $F_i$ . It is also assumed that since these

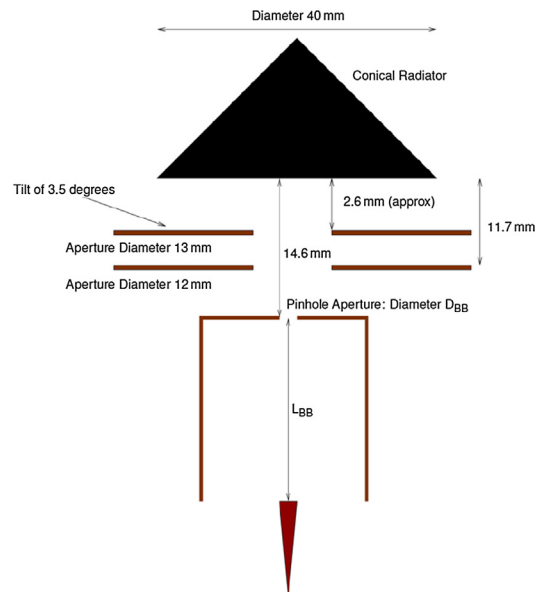


Fig. 3. Optical measurement system used by SRON to test the SAFARI pixels, from [4].

modes are coupling to the farfield blackbody source, that they have been re-normalised such that they represent the fraction of power coupled to that field for a given angle of incidence relative to the total power coupled to the mode for isotropic illumination of the antenna. For the  $i$ th mode, the fraction of the total power arriving at the pixel entrance is therefore calculated by integrating the re-normalised mode  $F_i$  over the angle subtended by the farfield pattern of the mode and the pinhole aperture  $\chi$ . This fraction is given by

$$\Gamma_i = \frac{\int_0^{2\pi} \int_{-\chi}^{\chi} F_i(\phi, \theta) d\theta d\phi}{\int_0^{2\pi} \int_{-\pi/2}^{\pi/2} F_i(\phi, \theta) d\theta d\phi}, \quad (19)$$

where  $\chi$  is given by  $\arctan\left(\frac{D_{BB}}{2L_{BB}}\right)$ . To calculate the total power lost from the system (the sum of the losses from all loss mechanisms), 6 is used, but the losses from each mode must be scaled to reflect the fraction of power that is actually excited in that mode. This results in an expression for the pixel efficiency that is given by

$$\eta_{\text{pixel}} = \frac{\sum_i (1 - \sigma_i^2) \Gamma_i}{\sum_i \Gamma_i}. \quad (20)$$

This expression gives the efficiency of the pixel relative to the power entering the pixel itself rather than the power entering the cavity, the latter being what is recorded during measurements. In order to account for this within the framework of a two port model, it was necessary to couple the calculated efficiencies to the SRON measurement system (the blackbody source) and compute the raw levels of power that would be recorded by the detectors, a figure which was measured experimentally.

The blackbody is assumed to have a surface area equal to that of the pinhole aperture. Eq. 21 is a standard Planck curve which gives the power density of the blackbody per unit wavelength, per unit area per steradian,

$$M_\lambda = \frac{2hc^2}{\lambda^5} \frac{1}{e^{\frac{hc}{\lambda kT}} - 1}. \quad (21)$$

The total power incident on the pixel aperture from this blackbody source,  $P_{BB}$ , is thus given by

$$P_{BB} = M_\lambda A_{\text{ap}} \Delta\lambda \Delta\Omega, \quad (22)$$

where  $A_{\text{ap}}$  is the area of the source and  $\Delta\lambda$  is the unit bandwidth.  $\Delta\Omega$  is the solid angle of the blackbody that covers the pixel aperture and is found by integrating across the angle subtended by the pixel and the pinhole aperture such that  $\Delta\Omega = \int_0^{2\pi} \int_0^\chi \sin\theta d\theta d\phi$ . The total power absorbed by the pixel is thus found by scaling the power incident on the pixel aperture,  $P_{BB}$  by the pixel efficiency given in 20 and also by the function  $\tau(\lambda)$  which represents the effect of the filters. The total power absorbed by the system and thus read out by the detectors is given by

$$P_{\text{absorbed}} = \eta_{\text{pixel}} P_{BB} \tau(\lambda). \quad (23)$$

### 3. Comparison of simulated and measured results

In this section, the analysis techniques outlined previously will be applied to the SAFARI pixel that was tested at SRON, with the simulated results compared to measured results. A schematic of the pixel tested is shown in Fig. 1, along with the relevant dimensions. The measurement system is shown in Fig. 3. The system was measured in three configurations which correspond to three sets of values for  $D_{BB}$  and  $L_{BB}$  the details of which are given in Table 1. These configurations effectively vary the angular size of the pinhole aperture, as seen by the pixel. The layer of tantalum that functions as the superconducting absorbing layer used by the TES coupled bolometer was modeled as an ohmic sheet with a surface impedance of 368  $\Omega/\text{sq}$  and the integrated power that would be read out by the detectors was calculated across the 35–70  $\mu\text{m}$  band (4.3–8.5 THz). Simulations of the experimental measurements

**Table 1**

Details of the system configuration for each of the 3 configurations.

Configuration #	$D_{BB}$	$L_{BB}$
1	0.9 mm	10.77 mm
2	0.5 mm	10.2 mm
3	1.4 mm	10.2 mm

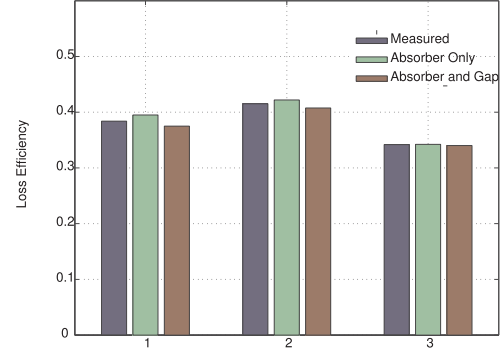


**Fig. 4.** Comparison of the loss efficiency for each configuration, for the three configurations of the system.

were carried out, including and excluding the 50  $\mu\text{m}$  free space gap, and compared to the measured values as illustrated in Fig. 4. Fig. 4 also shows the measured pixel efficiency. This was found by using the approach outlined in Section 2.5 to convert the power read out by transition edge sensors into an efficiency. Excellent agreement is noted between measurement and simulation for all three configurations of the system, validating the modelling technique. As expected the addition of the 50  $\mu\text{m}$  gap does not hugely impact upon the total power removed from the system, emphasising that the cavity is working well with most of the power being absorbed by the tantalum layer rather than diffracting out of the system. When the pixel is empty, most of the power is lost through the gap as the modes make many passes of the gap region as the system is a high Q-factor resonant cavity. On each subsequent pass of the gap the modes are diffracted more and so more power is lost from the centre of the pixel. When an absorbing layer is added, significantly less power is available to traverse the gap more than once, as the majority of power is absorbed by the tantalum on the first pass, resulting in less power being lost due to diffraction.

#### 3.1. The effect of the free space gap

In this section the effect on the cavity performance of the free space gap is examined.

The system is now examined with the gap present, but in the absence of the absorber (referred to as an open, empty pixel). Physically this is very different to having an absorber present as now the system behaves like a high Q-factor resonant cavity that is not damped. It is clear from Fig. 5 that the overall trend is for the total power lost to decrease with increasing wavelength. With the gap width fixed at 50  $\mu\text{m}$ , it appears larger at the shorter wavelength end of the band. More diffraction will therefore occur at these wavelengths, resulting in more losses due to the gap. It is expected therefore that as the effective size of the gap changes in terms of wavelength, that resonant features will be noted in the amount of power leaked, something which is clear from Fig. 5 where resonant dips are clearly visible at specific wavelengths.

With both the gap and the absorber included, the simulations were repeated. It is important to note again that since SCATTER models two port systems, the power 'missing' from the system is the power lost via the gap summed with the power lost via the absorber. It is also important to note that the overall system is not a linear combination of an

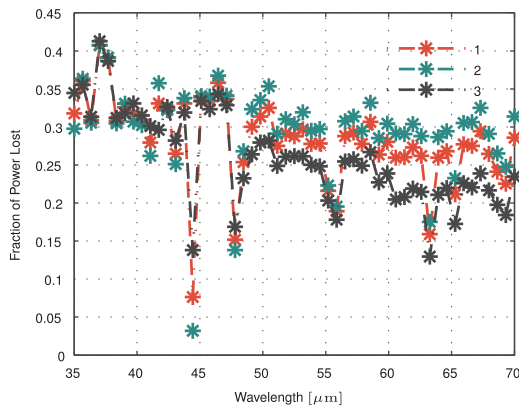


Fig. 5. Fractional power leaked for an open (50  $\mu\text{m}$  free space gap included), empty pixel over a 35–70  $\mu\text{m}$  band in each of the three measurement configurations.

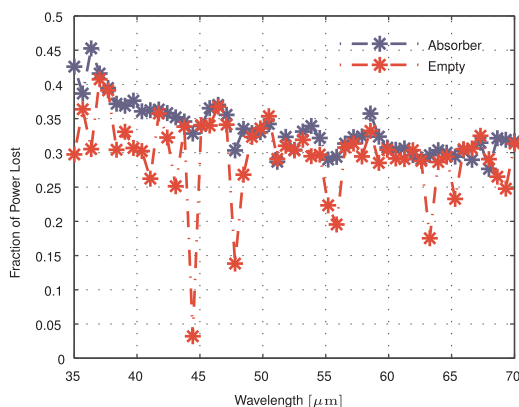


Fig. 6. Comparison of power lost from the system over a 35–70  $\mu\text{m}$  band in measurement configuration 2, with and without an absorbing layer for a free space gap of 50  $\mu\text{m}$ .

open, empty pixel and a closed pixel with an absorber. Adding the power lost in both cases will not return the total power lost when an open pixel with an absorber is run, as the cavities have different Q factors in each case.

Fig. 6 shows the total power lost from the system as a function of wavelength for configuration 2 (see Table 1), with similar results obtained in the other two cases. When an absorber is included, the same trend is still noted whereby the leaked power decreases with increasing wavelength. The system also exhibits fewer resonant peaks, as the absorber dampens the resonant nature of the cavity/gap system. Both systems show similar levels of total power loss, but this does not imply that the absorber has little impact. As stated, the addition of the absorber fundamentally changes the system, so although the total levels of power not returned to the entrance port remain similar, the sources of the losses are entirely different in the two cases. With the absorber present, most of each mode (in terms of power) will only traverse the gap once as they will undergo two passes of the absorber before exiting the cavity back into the gap region. Most of the power will therefore be absorbed, with very little power available for subsequent passes of the gap which is where the power is leaked from in the case of the empty pixel. This again shows that the cavity is working well, with the majority of the power being absorbed when an absorbing layer is present.

#### 4. Conclusion

For future far-infrared missions, it is necessary to develop highly sensitive multi-mode pixels. Such pixels have been designed, manufactured and tested by SRON Groningen with a view to being used for

the proposed SAFARI instrument. In this paper we have outlined the development and verification of an efficient analysis tool, based on the mode-matching technique, that can be applied to these pixels. We applied the developed tool to a prototype SAFARI pixel, including additional modifications made to account for the SRON measurement system. Excellent agreement was obtained between the simulations and the SRON measurements. The impact of the free space gap on the efficiency of the pixel was also investigated.

The modifications made to the mode-matching technique have allowed the expedient and accurate simulation of complex test pixels containing cavities, free space gaps and absorbers for future far-infrared missions, and can be used in the future design, optimisation and experimental verification and analysis of such pixels.

#### Declaration of Competing Interest

The authors declare that they have no known competing financial interests or personal relationships that could have appeared to influence the work reported in this paper.

#### Acknowledgements

The authors would like to acknowledge funding from the European Space Agency under the Strategic Initiative for Irish Industry, Academia and Research Institutes, and the Irish Research Council (formerly IRCSET) under the EMBARK scheme.

#### References

- [1] G. Pilbratt, T. Riedinger, G. Passvogel, G. Crone, D. Doyle, et al., Herschel space observatory - an ESA facility for far-infrared and submillimetre astronomy, *Astron. Astrophys.* 518 (2010) 118–173, <https://doi.org/10.1051/0004-6361/201014759>.
- [2] P. Roelfsema, M. Giard, F. Najarro, K. Wafelbakker, W. Jellema, et al., Safari new and improved: extending the capabilities of spica's new imaging spectrometer, *SPIE Proceedings 9143, Space Telescopes and Instrumentation 2014: Optical, Infrared and Millimeter Wave*, 2014.
- [3] W. Jellema, D. van Loon, D. Naylor, P. Roelfsema, The safari far-infrared instrument for the spica space telescope, in: *Light, Energy and the Environment 2018 (E2, FTS, HISE, SOLAR, SSL)*, Optical Society of America, 2018, p. FW3B.3. doi:10.1364/FTS.2018.FW3B.3. <http://www.osapublishing.org/abstract.cfm?URI=FTS-2018-FW3B.3>.
- [4] M. Audley, G. de Lange, M. Ranjan, J. Gao, et al., Measurements of the optical performance of prototype TES bolometers for SAFARI, *J. Low Temp. Phys.* 176 (5) (2014) 755–760, <https://doi.org/10.1007/s10909-013-0984-5>.
- [5] M. Audley, G. de Lange, J. Gao, R. Khosropanah, et al., Optical performance of an ultra-sensitive horn-coupled transition-edge-sensor bolometer with hemispherical backshort in the far infrared, *Rev. Sci. Instrum.* 87(4). doi: 10.1063/1.4945302.
- [6] A. Olver, P. Clarricoats, A. Kishk, L. Shafai, *Microwave Horns and Feeds*, IEEE, 1994.
- [7] R. Colgan, J. Murphy, B. Maffei, C. O'Sullivan, R. Wylde, P. Ade, Modelling few-modded horns for far-ir space applications, *Proc. 11th International Symposium on Space Terahertz Technology*, Ann Arbor, Michigan, 2000.
- [8] J. Murphy, S. Doherty, N. Trappe, C. Bracken, T. Peacocke, C. O'Sullivan, New developments in waveguide mode-matching techniques for far-infrared astronomy, vol. 8261, 2012, pp. 12. doi: 10.1117/12.908068.
- [9] C.N. Thomas, S. Withington, Optical modeling techniques for multimode horn-coupled power detectors for submillimeter and far-infrared astronomy, *J. Opt. Soc. Am. A* 30 (8) (2013) 1703–1713, <https://doi.org/10.1364/JOSAA.30.001703> <http://josaa.osa.org/abstract.cfm?URI=josaa-30-8-1703>.
- [10] S. Withington, M. Hobson, R. Berry, Representing the behaviour of partially coherent optical systems by using overcomplete basis sets, *J. Opt. Soc. Am.* 21 (2) (2004) 207–217, <https://doi.org/10.1364/JOSAA.21.000207>.
- [11] D. McCarthy, N. Trappe, J. Murphy, C. O'Sullivan, M. Gradziel, et al., The optimisation, design and verification of feed horn structures for future cosmic microwave background missions, *Infrared Phys. Technol.* 76 (2016) 32–37, <https://doi.org/10.1016/j.infrared.2015.12.014>.
- [12] P. Goldsmith, *Quasioptical Systems: Gaussian Beam Quasioptical Propagation and Applications*, Wiley-IEEE Press, 1997.
- [13] N. Trappe, J. Murphy, S. Withington, W. Jellema, Gaussian beam mode analysis of standing waves between two coupled corrugated horns, *IEEE Trans. Antennas Propag.* 53 (5) (2005) 1755–1761, <https://doi.org/10.1109/TAP.2005.846453>.
- [14] D. McCarthy, N. Trappe, S. Doherty, J. Murphy, et al., Analysis and optical characterisation of bolometric integrating cavities including a free space gap in the waveguide structure, *Proc. 9th European Conference on Antennas and Propagation (EuCAP)*, Lisbon, 2015.